PERGAMON

International Journal of Solids and Structures 39 (2002) 983–1002

INTERNATIONAL JOURNAL OF SOLIDS and STRUCTURES

www.elsevier.com/locate/ijsolstr

Instability and localized deformation in polycrystalline solids under plane-strain tension

K. Inal [a], P.D. Wu [b], K.W. Neale [a,*]

[a] *Department of Civil Engineering, University of Sherbrooke, Sherbrooke, Que., Canada J1K 2R1*
[b] *Alcan International Limited, Kingston R&D Centre, Kingston, Ont., Canada K7L 5L9*

Received 14 November 2000

Abstract

In this paper we investigate the nonuniform and localized deformation of a polycrystalline aggregate under plane-strain tension. A finite element analysis based on rate-dependent crystal plasticity has been developed to simulate large strain behaviour. Each material point in the specimen is considered to be a polycrystalline aggregate of a large number of FCC grains. The Taylor theory of crystal plasticity is assumed. This analysis accounts for initial textures, as well as texture evolution during large plastic deformations. The numerical analysis incorporates certain parallel computing features. Simulations have been carried out for a commercial aluminium sheet alloy (AA3004-H19), and the effects of various parameters on the formation and prediction of localized deformation (in the form of necking and/or shear bands) are examined.

Keywords: Crystal plasticity; Localized deformation; Necking; Shear bands

1. Introduction

In early stages of tensile straining, polycrystal aggregates of ductile metals and alloys exhibit deformation patterns which, on a macroscopic scale are essentially homogeneous. With continued straining, however, the homogeneous deformation pattern is observed to change to a nonhomogeneous one, generally through the onset of diffuse necking (Hutchinson and Neale, 1977, 1978a,b) and/or localized shearing (Peirce et al., 1982). Failure usually ensues either by necking down to a 'chisel edge' or by rupture within intense shear bands.

There are two main methods of analysis for plastic instability predictions. For a rate-insensitive solid, plastic instability occurs either as a bifurcation state for a perfect specimen or as an imperfection-triggered localization. For rate-sensitive materials, bifurcation is effectively excluded, but small material inhomogeneities can still result in localization. In the limit of low material rate sensitivity, the localization strain predicted for a given initial inhomogeneity is practically identical to that predicted for the corresponding rate-insensitive solid, while for high-rate sensitivity, localization is retarded considerably.

* Corresponding author.
E-mail address: kenneth.neale@courrier.usherb.ca (K.W. Neale).

0020-7683/02/$ - see front matter
PII: S0020-7683(01)00246-3

Peirce et al. (1982) presented finite element (FE) calculations for nonuniform deformation modes in ductile single crystals, based on a rate-independent constitutive model for crystallographic slip. Their analysis, however, highlighted inherent limitations of the rate-independent idealization of crystalline slip. As a result of these limitations, Peirce et al. (1983) presented the constitutive theory for crystalline slip for rate-dependent material response and simulated large strain tension tests of single crystals. Their results provided a general understanding of the roles of rate sensitivity and lattice kinematics in the development of localized modes of deformation.

More recently, Zikry and Nemat-Nasser (1990) have studied numerically the phenomenon of shear banding in a FCC single crystal undergoing plane-strain tensile deformations at high strain rates. Harren et al. (1988) have analysed shear band formation during plane-strain compression of single crystals and polycrystals. The problem of the initiation and growth of dynamic shear bands in a FCC single crystal deformed in simple compression was presented by Zhu and Batra (1993).

Simulations with single crystals provide some understanding into the micromechanics of localized deformation in polycrystalline materials. However, the common metals of industrial practice are polycrystalline aggregates and there are few FE analyses for polycrystals (especially analyses based on Taylor assumptions) due to their significantly large computational requirements.

In this paper, the nonuniform deformation of polycrystals subjected to plane-strain tension has been simulated using a polycrystal model-based FE code. Many researchers (Harren and Asaro, 1989a; Kalidindi et al., 1991; Kaidindi and Anand, 1994) have shown that the Taylor model for polycrystalline materials is in reasonably good agreement with experiments, both for the evolution of textures as well as for the overall stress–strain response of single-phase FCC materials. For this reason, and also for its relative simplicity in computations, a Taylor-type polycrystal model has been implemented into our FE code. The FE analysis incorporates certain parallel computing algorithms to distribute data between the processors of an IBM SP3 parallel computer. We first recapitulate the polycrystal constitutive model employed. Then the FE formulation is briefly presented. In the last section we present results for a commercial aluminium sheet alloy (AA3004-H19), and discuss the effects of various parameters on the formation of localized deformation bands.

2. Constitutive model

The polycrystal plasticity model described by Asaro and Needleman (1985) and employed by Wu et al. (1996a) is used in our analysis. Accordingly, the total deformation of a crystallite is the result of two distinct physical mechanisms: crystallographic slip due to dislocation motion on the active slip systems, and elastic lattice distortion. Within a FCC crystal, plastic deformation occurs by crystallographic slip on the 12 $\{1\,1\,1\}\langle 1\,1\,0\rangle$ slip systems where the slip planes are the $\{1\,1\,1\}$ crystallographic planes with normals $\boldsymbol{m}$, and the $\langle 1\,1\,0\rangle$ directions are the shear directions with slip vectors $\boldsymbol{s}$. Plastic deformation is envisaged to occur as a set of plastic simple shears along the various slip systems, leaving the lattice and the slip system vectors $(\boldsymbol{s}_{(\alpha)}, \boldsymbol{m}_{(\alpha)})$ not only essentially undistorted, but also unrotated. (The brackets for the subscripts α indicate that α is not a tensor index and ranges from one to the total number of slip systems.) Next, the material and lattice are considered to deform elastically and rotate rigidly from the plastically deformed state to the current configuration.

The deformation gradient $\boldsymbol{F}$ is written as:

$$\boldsymbol{F} = \boldsymbol{F}^{*}\boldsymbol{F}^{\mathrm{p}} \tag{1}$$

where $\boldsymbol{F}^{\mathrm{p}}$ consists solely of crystallographic slipping along the specific slip systems, while the elastic deformation and any rigid body rotation is embodied in $\boldsymbol{F}^{*}$. From Eq. (1), the spatial gradient of velocity can be written as

$$\boldsymbol{L} = \dot{\boldsymbol{F}}\boldsymbol{F}^{-1} = \boldsymbol{L}^{*} + \boldsymbol{L}^{\mathrm{p}} \tag{2}$$

where

$$\boldsymbol{L}^{*} = \dot{\boldsymbol{F}}^{*}\boldsymbol{F}^{*^{-1}}, \qquad \boldsymbol{L}^{\mathrm{p}} = \boldsymbol{F}^{*}(\dot{\boldsymbol{F}}^{\mathrm{p}}\boldsymbol{F}^{\mathrm{p}^{-1}})\boldsymbol{F}^{*^{-1}} \tag{3}$$

Taking symmetric and antisymmetric parts of the above relations leads to the elastic and plastic strain rates $\boldsymbol{D}^{*}$ and $\boldsymbol{D}^{\mathrm{p}}$, the so-called plastic spin $\boldsymbol{W}^{\mathrm{p}}$, and the spin $\boldsymbol{W}^{*}$ associated with the rigid lattice rotation

$$\boldsymbol{D} = \boldsymbol{D}^{*} + \boldsymbol{D}^{\mathrm{p}}, \qquad \boldsymbol{W} = \boldsymbol{W}^{*} + \boldsymbol{W}^{\mathrm{p}} \tag{4}$$

The vectors $\boldsymbol{s}_{(\alpha)}$ and $\boldsymbol{m}_{(\alpha)}$ are regarded as lattice vectors so that they stretch and rotate by

$$\boldsymbol{s}^{*}_{(\alpha)} = \boldsymbol{F}^{*}\boldsymbol{s}_{(\alpha)}, \quad \boldsymbol{m}^{*}_{(\alpha)} = \boldsymbol{m}_{(\alpha)}\boldsymbol{F}^{*^{-1}} \tag{5}$$

By introducing the following symmetric and skewsymmetric tensors for each slip system α

$$\boldsymbol{P}_{(\alpha)} = \tfrac{1}{2}[\boldsymbol{s}^{*}_{(\alpha)} \otimes \boldsymbol{m}^{*}_{(\alpha)} + \boldsymbol{m}^{*}_{(\alpha)} \otimes \boldsymbol{s}^{*}_{(\alpha)}] \tag{6}$$

$$\boldsymbol{W}_{(\alpha)} = \tfrac{1}{2}[\boldsymbol{s}^{*}_{(\alpha)} \otimes \boldsymbol{m}^{*}_{(\alpha)} - \boldsymbol{m}^{*}_{(\alpha)} \otimes \boldsymbol{s}^{*}_{(\alpha)}] \tag{7}$$

the plastic strain rate and spin for the crystal can be respectively written as

$$\boldsymbol{D}^{\mathrm{p}} = \sum_{\alpha} \boldsymbol{P}_{(\alpha)}\dot{\gamma}_{(\alpha)}, \qquad \boldsymbol{W}^{\mathrm{p}} = \sum_{\alpha} \boldsymbol{W}_{(\alpha)}\dot{\gamma}_{(\alpha)} \tag{8}$$

where $\dot{\gamma}_{(\alpha)}$ is the shear rate on the slip system α.

The elastic constitutive equation for a crystal is specified by

$$\overset{\nabla}{\boldsymbol{\tau}}{}^{*} = \dot{\boldsymbol{\tau}} - \boldsymbol{W}^{*}\boldsymbol{\tau} + \boldsymbol{\tau}\boldsymbol{W}^{*} = \mathsf{L}\boldsymbol{D}^{*} \tag{9}$$

where $\overset{\nabla}{\boldsymbol{\tau}}{}^{*}$ is the Jaumann rate of the Kirchhoff stress tensor $\boldsymbol{\tau}$ based on the lattice rotations, and L is the tensor of the elastic moduli. These moduli are based on the anisotropic elastic constants of the FCC crystals and thus exhibit the appropriate cubic symmetry.

In order to express the constitutive relation (9) in terms of the Jaumann rate $\overset{\nabla}{\boldsymbol{\sigma}}$ of the Cauchy stress $\boldsymbol{\sigma} = \det(\boldsymbol{F})^{-1}\boldsymbol{\tau}$, based on the continuum slip $\boldsymbol{W}$, we introduce a second-order tensor $\boldsymbol{R}_{(\alpha)}$ for each slip system as follows

$$\boldsymbol{R}_{(\alpha)} = \mathsf{L}\boldsymbol{P}_{(\alpha)} + \boldsymbol{W}_{(\alpha)}\boldsymbol{\sigma} - \boldsymbol{\sigma}\boldsymbol{W}_{(\alpha)} \tag{10}$$

Using Eqs. (4)–(8) and (10), the constitutive law (9) can be rewritten in the form

$$\overset{\nabla}{\boldsymbol{\sigma}} = \mathsf{L}\boldsymbol{D} - \dot{\boldsymbol{\sigma}}^{0} - \boldsymbol{\sigma}\,\mathrm{tr}\,\boldsymbol{D} \tag{11}$$

where $\dot{\boldsymbol{\sigma}}^{0}$ is a viscoplastic type stress rate defined by

$$\dot{\boldsymbol{\sigma}}^{0} = \sum_{\alpha} \boldsymbol{R}_{(\alpha)}\dot{\gamma}_{(\alpha)} \tag{12}$$

The slip rates to be substituted into Eq. (12) are taken to be governed by the power law expression

$$\dot{\gamma}_{(\alpha)} = \dot{\gamma}_{(0)}\,\mathrm{sgn}\,\tau_{(\alpha)}\left|\frac{\tau_{(\alpha)}}{g_{(\alpha)}}\right|^{1/m} \tag{13}$$

where $\dot{\gamma}_{(0)}$ is a reference shear rate taken to be the same for all the slip systems, $\tau_{(\alpha)} = \boldsymbol{P}_{(\alpha)}{:}\boldsymbol{\sigma}$ is the resolved shear stress on slip system α; $g_{(\alpha)}$, its hardness and m, the strain-rate sensitivity index. The $g_{(\alpha)}$ characterize the current strain-hardened state of all slip systems. The rate of increase of the function $\dot{g}_{(\alpha)}$ is defined by the hardening law:

$$\dot{g}_{(\alpha)} = \sum_{\beta} h_{(\alpha\beta)} |\dot{\gamma}_{(\beta)}| \tag{14}$$

where $g_{(\alpha)}(0)$ is the initial hardness, taken to be a constant τ_0 for each slip system, and $h_{(\alpha\beta)}$ are the hardening moduli. The form of these moduli is

$$h_{(\alpha\beta)} = q_{(\alpha\beta)} h_{(\beta)} \quad \text{(no sum on } \beta) \tag{15}$$

where $h_{(\beta)}$ is a single slip hardening rate and $q_{(\alpha\beta)}$ is the matrix describing the latent hardening behaviour of the crystallite.

Asaro and Needleman (1985), among others, simply take each $g_{(\alpha)}$ to depend on the accumulated sum, γ_a, of the slips; i.e.

$$g_{(\alpha)} = g_{(\alpha)}(\gamma_a), \qquad \gamma_a = \int_0^t \sum_{\alpha} |\dot{\gamma}_{(\alpha)}| \, \mathrm{d}t \tag{16}$$

Based on measurements of strain hardening of single crystals of aluminium alloys by Chang and Asaro (1981), the following slip hardening rate was used by Asaro and coworkers:

$$h_\beta = h_s + (h_0 - h_s) \operatorname{sech}^2 \left\{ \left(\frac{h_0 - h_s}{\tau_s - \tau_0} \right) \gamma_a \right\} \tag{17}$$

where h_0 and h_s are the system's initial and asymptotic hardening rates. If $h_s = 0$, then τ_s represents the saturation value of the shear stress.

The response of a polycrystal comprised of many grains is obtained by invoking the Taylor assumption. Thus, at a material point representing a polycrystal of N grains, the deformation in each grain is taken to be identical to the macroscopic deformation of the continuum. Furthermore, the macroscopic values of all quantities, such as stresses, stress rates and elastic moduli, are obtained by averaging their respective values over the total number of grains at the particular material point.

3. Finite element implementation

A FE procedure based on a Lagrangian formulation of the field equations using convected coordinates has been developed. Thus if $\boldsymbol{g}_i$ are the base vectors in the undeformed configuration corresponding to the convected coordinates x_i the deformed base vectors are $\boldsymbol{G}_i = \boldsymbol{F}\boldsymbol{g}_i$. The initial, undeformed configuration of the body with volume V and surface S is used as a reference. Then, for quasi-static deformations and in the absence of body forces, the equilibrium equations are expressed through the virtual work condition

$$\int_V \tau^{ij} \, \delta\eta_{ij} \, \mathrm{d}V = \int_S T^i \, \delta u_i \, \mathrm{d}S \tag{18}$$

for arbitrary variations of the displacement components u_i and corresponding variations of the components η_{ij} of the Lagrangian strain tensor. Here, τ^{ij} are the components on the undeformed basis of the second Piola–Kirchhoff tensor and T^i are the corresponding traction vectors.

In the linear incremental problem, we suppose the current state of approximate equilibrium to be known at time t. To determine the equations for the field quantity rates, Eq. (18) is expanded in a Taylor series about the time t to yield (Needleman and Tvergaard, 1984)

$$\Delta t \int_V \left(\dot{\tau}^{ij} \, \delta\eta_{ij} + \tau^{ij} \dot{u}^k_{,i} \, \delta u_{k,j} \right) \mathrm{d}V = \Delta t \int_S \dot{T}^i \, \delta u_i \, \mathrm{d}S - \left[\int_V \tau^{ij} \, \delta\eta_{ij} \, \mathrm{d}V - \int_S T^i \, \delta u_i \, \mathrm{d}S \right] \tag{19}$$

The last term on the right of Eq. (19) serves as an equilibrium correction if equilibrium in the current state is only approximate.

3.1. Problem formulation

A specimen submitted to uniaxial tension has been modelled under the assumption of plane-strain conditions. The initial length of the specimen is $2L_0$ and its initial thickness is $2(h_0 + \Delta h_0)$ where $2h_0$ is the average thickness and $2\Delta h_0$ is the initial thickness inhomogeneity.

When x_1 and x_3 are assumed to coincide with the rolling and normal directions of the sheet, respectively, material orthotropy and symmetry with respect to these axes can be assumed. As a result, only one quarter of the specimen needs to be considered in the numerical solution (Fig. 1). This mesh consists of four-node quadrilateral elements, made up of four 'crossed' constant strain triangular sub-elements. In presenting results, the quadrilateral is regarded as the basic element, and when reporting values of the field quantities the average value of the triangles is associated with the centroid of the quadrilateral (Wu and Van der Giessen, 1996b).

With the tensile axis aligned in the x_1 direction, the boundary conditions on the quadrant are

$$\begin{aligned} &u_3 = 0 \quad \text{at } x_3 = 0 \\ &u_1 = 0 \quad \text{at } x_1 = 0 \\ &\dot{u}_1 = V \text{ (applied velocity)} \quad \text{at } x_1 = L_0 \end{aligned} \tag{20}$$

and the end of the specimen; $x_1 = L_0$, is considered to be shear free.

The initial thickness imperfection Δh_0 follows that of Tvergaard et al. (1981), and is given by

$$\Delta h_0 = h_0\left[-\xi_1 \cos(\pi x^2/L_0) + \xi_2 \cos(p\pi x^2/L_0)\right] \tag{21}$$

where ξ_1 and ξ_2 are prescribed imperfection amplitudes and $p(>1)$ is the wave number.

3.2. Parallel computing

In general, Taylor-type polycrystal models are ideally suited for the parallelization of the computational procedures. Especially, when CPU time is considered, the simulations fall in the category of "embarrassingly parallel" (Sorensen and Andersen, 1995) applications, and they provide significant computational improvements. However, such "embarrassingly parallel" applications are strictly feasible only if the total program size fits within a single processor of the parallel computer. This was not the case for the simulations presented in this paper, and it was necessary to implement the polycrystal FE model in a data parallel form as described by Beaudoin et al. (1993).

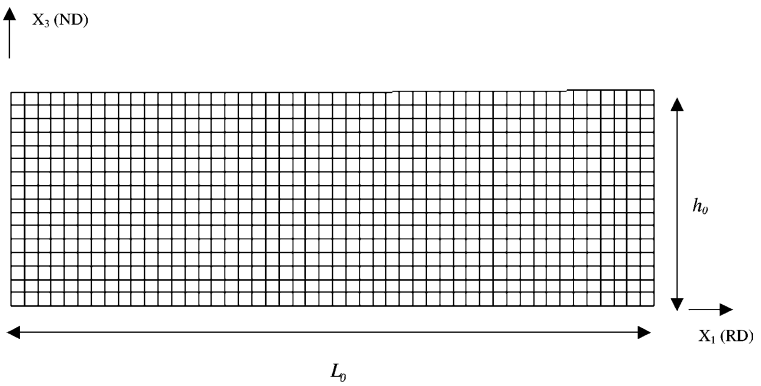

Fig. 1. FE mesh used in simulations.

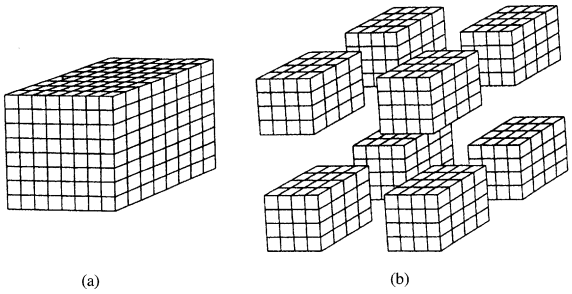

Fig. 2. Parallel data implementation.

The parallel algorithms used in our simulations are designed to distribute data on the microscopic level (crystal data) over the processors of an IBM SP3 supercomputer (Inal et al., 2000a). To illustrate this, consider a simulation with a total number N of crystals (Fig. 2a). The global crystal data is distributed between the processors (Fig. 2b) such that each processor runs a part of the global program for N/A crystals where A is the total number of processors used in the simulation.

The macroscopic values of all quantities such as stresses, stress rates and elastic moduli are obtained by collective communication between the processors using the message passing interface library. As a result, each processor has its own microscopic data; however, all of the processors have the same macroscopic data. We should mention that the total number of crystals should be distributed as evenly as possible between the processors. Otherwise the large difference in the number of crystals per processor adversely affects the CPU time per processor, and in such cases blocking commands (which are costly in terms of CPU) are required during communication between processors. To avoid this the parallel algorithms developed here distribute the crystals as evenly as possible among the available processors.

The parallel computing algorithms which we have developed are essential for the simulations presented in this paper. These parallel sub-routines enable simulations with sufficiently fine meshes necessary to capture the key features of localized deformation for the aluminium alloy analysed. Note that, each element in our simulations has four integration points and each integration point is considered to represent a polycrystal aggregate comprised of 380 grains. For this case, the maximum number of elements that can be used in a simulation with a sequential computer such as an IBM RISC 6000 is 35 while the majority of the simulations (performed on the IBM SP3 parallel computer) presented in this paper consist of 768 elements.

4. Results and discussion

The initial texture (represented by 380 crystals) of the aluminium sheet alloy AA3004-H19 is presented in Fig. 3. Here X_1, X_2 and X_3 refer to the rolling, transverse and the normal directions of the sheet, respectively. Various studies have been presented investigating the significance of the number of grains used to represent an initial texture (Harren et al., 1989b; Van der Giessen and Neale, 1993; Wu et al., 1997). The initial texture used in this study was provided by the Kingston Research and Development Centre of Alcan International, where a representation of 380 grains was considered to be sufficient to capture the components of a typical rolling texture and to assure orthotropic material symmetry.

The values of the material properties used in the simulations are,

$$\tau_0 = 95 \text{ MPa}, \quad h_0/\tau_0 = 1.2, \quad \tau_s/\tau_0 = 1.16, \quad h_s/\tau_0 = 0, \quad q = 1.0 \tag{22}$$

These properties were obtained by fitting the uniaxial stress–strain curve obtained by crystal plasticity to the uniaxial stress–strain curve measured experimentally (Inal et al., 2000b). The slip system reference

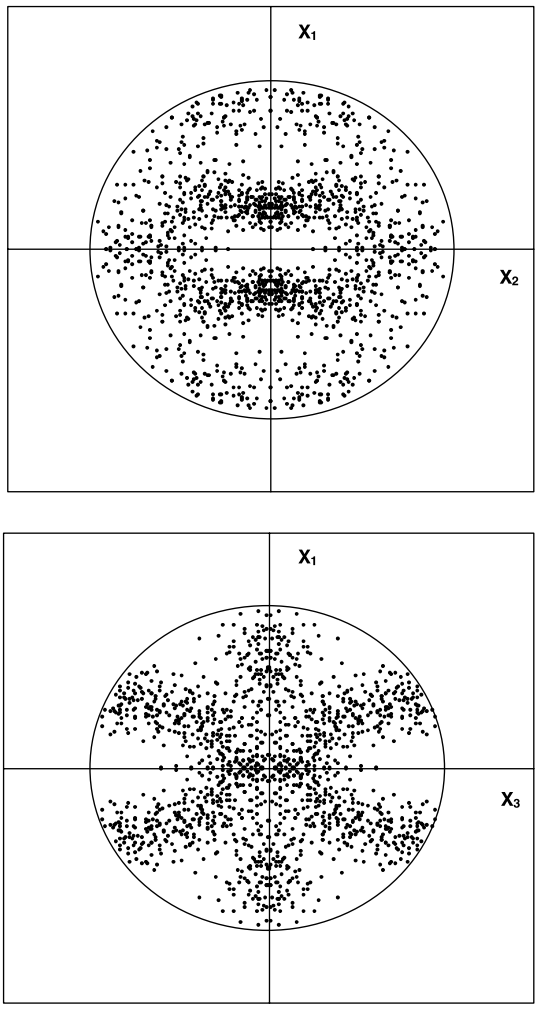

Fig. 3. Initial texture of AA3004-H19 represented by {1 1 1} stereographic pole figure.

plastic shearing rate $\dot{\gamma}_0$ and the slip rate sensitivity parameter m are taken as $\dot{\gamma}_0 = 0.001\ \mathrm{s}^{-1}$ and $m = 0.002$, respectively with the crystal elastic constants taken as $C_{11} = 206$ GPa, $C_{12} = 118$ GPa and $C_{44} = 54$ GPa.

4.1. A typical result

The specimen is stretched under plane-strain tension by applying the boundary conditions defined in Eq. (20). The initial aspect ratio of the specimen considered in this study is $L_0/h_0 = 3$ and the FE discretization takes the form of 768 quadrilaterals with 16 elements in x_3 direction and 48 elements in x_1 direction (Fig. 1). The initial thickness imperfection is given by Eq. (21), with $\xi_1 = 0.42 \times 10^{-2}$, $\xi_2 = 0.24 \times 10^{-2}$, and a wave number $p = 2$.

The normalized nominal stress $(\sigma_{\mathrm{NOM}}/\tau_0)$–elongation (U/L_0) response is presented in Fig. 4. This curve indicates that the normalized nominal stress reaches a maximum around $U/L_0 = 0.055$, and then begins to decrease. The deformation patterns at various normalized elongations are shown in Fig. 5. Fig. 5a shows

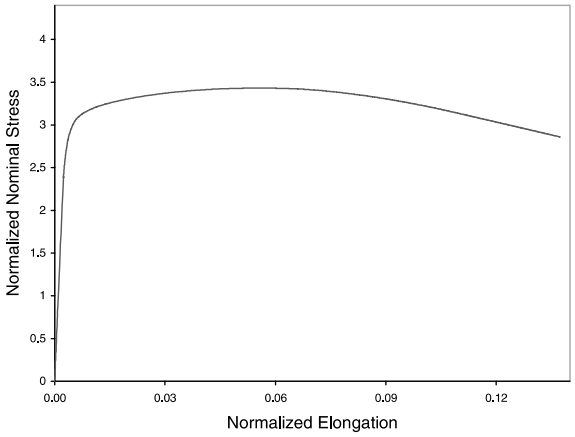

Fig. 4. Normalized nominal stress–elongation curve.

the deformed mesh after the maximum normalized nominal stress, at $U/L_0 = 0.07$, where a very light diffuse neck has formed. Evidence of shear bands that cross at the specimen centre can be observed in Fig. 5b, where $U/L_0 = 0.10$, but they are most fully developed at $U/L_0 = 0.13$ as shown in Fig. 5c.

A more quantitative representation of shear band development is presented in Fig. 6, where contours of true strain (in the loading direction) are plotted versus the normalized elongation. Fig. 6a corresponds to Fig. 5a, where $U/L_0 = 0.07$. Although the strain pattern is slightly nonuniform, an inhomogeneity corresponding to the early stages of necking can be observed since the highest strains are at the centre of the specimen.

A shear band pattern is evident in Fig. 6b, which shows contour plots at $U/L_0 = 0.10$. Although little additional straining has occurred towards the end of the specimen as compared to Fig. 6a, strain has began to concentrate in a well-defined band (represented by the 0.21 contour) nearer the specimen centre.

Fig. 6c shows the fully developed shear band at $U/L_0 = 0.13$. The strains in the shear band exceed 0.4 although the overall normalized extension is $U/L_0 = 0.13$. While there is very little deformation occurring outside the band, a large amount of shear is accumulating within the well-defined shear band (represented by the 0.4 contour).

4.2. Mesh sensitivity

Shear band localization phenomena are notorious for sometimes exhibiting a pathological mesh sensitivity. However, as demonstrated by Needleman (1988), this is not necessarily the case for our type of simulations since the inherent mesh sensitivity of the rate-independent theory can be eliminated by a rate-dependent formulation such as the one in this study. Nevertheless, the selection of proper mesh does require proper attention.

Mesh sensitivity analyses were first performed by keeping the element aspect ratio constant and increasing the element number in the necking area which is considered as the first 1/3 of the specimen as defined in Fig. 7. Thus, all mesh sizes described in this section refer to the size of the mesh at the necking area. For the first set of analyses, simulations were performed with meshes consisting of 12×12, 16×16 and 24×24 elements, respectively.

The numerical results show that, the overall stress–strain curves for all three meshes are nearly identical in terms of strain hardening and saturation (Fig. 8). Once softening occurs, finer meshes demonstrate slightly stronger softening effects. Fig. 9 presents contours of true strain (in the loading direction) for the

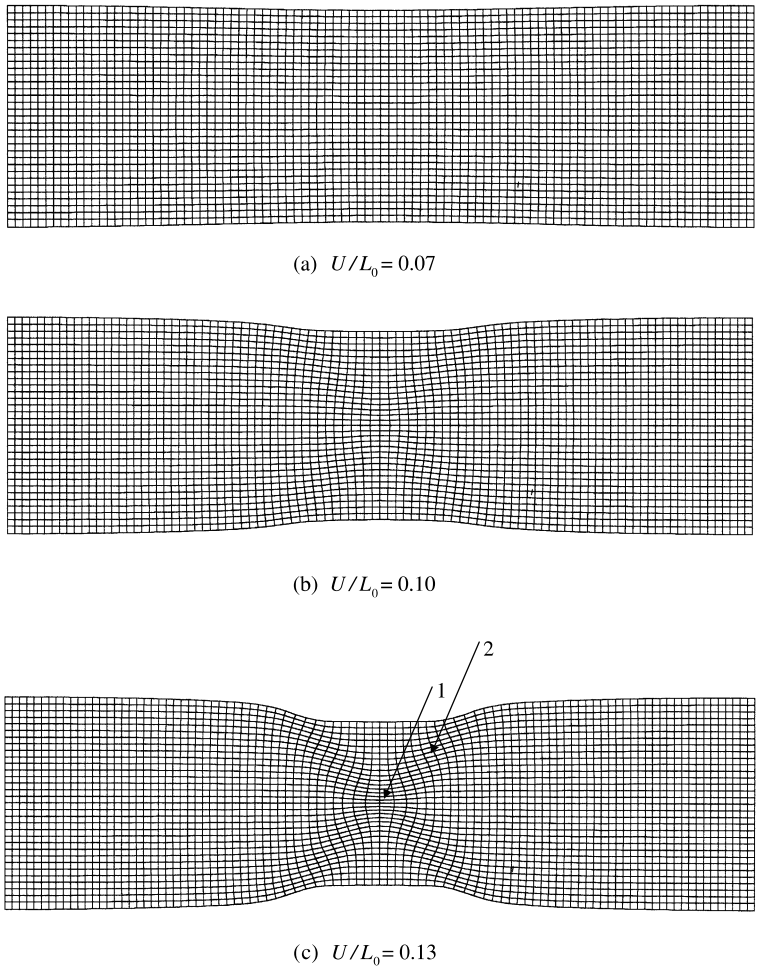

(a) $U/L_0 = 0.07$

(b) $U/L_0 = 0.10$

(c) $U/L_0 = 0.13$

Fig. 5. Deformed meshes at various elongation levels.

three meshes considered at $U/L_0 = 0.13$. Our results show that the initiation and propagation of shear bands are not sensitive to the meshes considered; for all cases, localized deformation in the form of a shear band passing through the centre of the specimen is formed at approximately 47° to the loading direction. Although it does not have a significant impact on localized deformation, it is also observed that, the finer the mesh, the narrower and stronger the shear band.

We next present mesh sensitivity analyses where the element aspect ratio a/b (where a and b are the lengths of an element in the x_1 and x_3 directions, respectively, in the necking area) has been changed. Fig. 10 presents the nominal stress–normalized elongation curves for simulations with element aspect ratios of 2.0 (32 elements in the x_3 direction, 16 elements in the x_1 direction), 1.0 (24 elements each in the x_3 and x_1 directions), and 0.5 (16 elements in the x_3 direction, 32 elements in the x_1 direction), respectively. Once again, all curves are nearly the same with regard to strain hardening and saturation. After saturation, a stronger softening effect is observed for simulations having smaller element aspect ratios.

The deformation patterns for the above three simulations are compared in Fig. 11 where contours of true strain (in the loading direction) are plotted at $U/L_0 = 0.13$. The simulations show that the shear bands

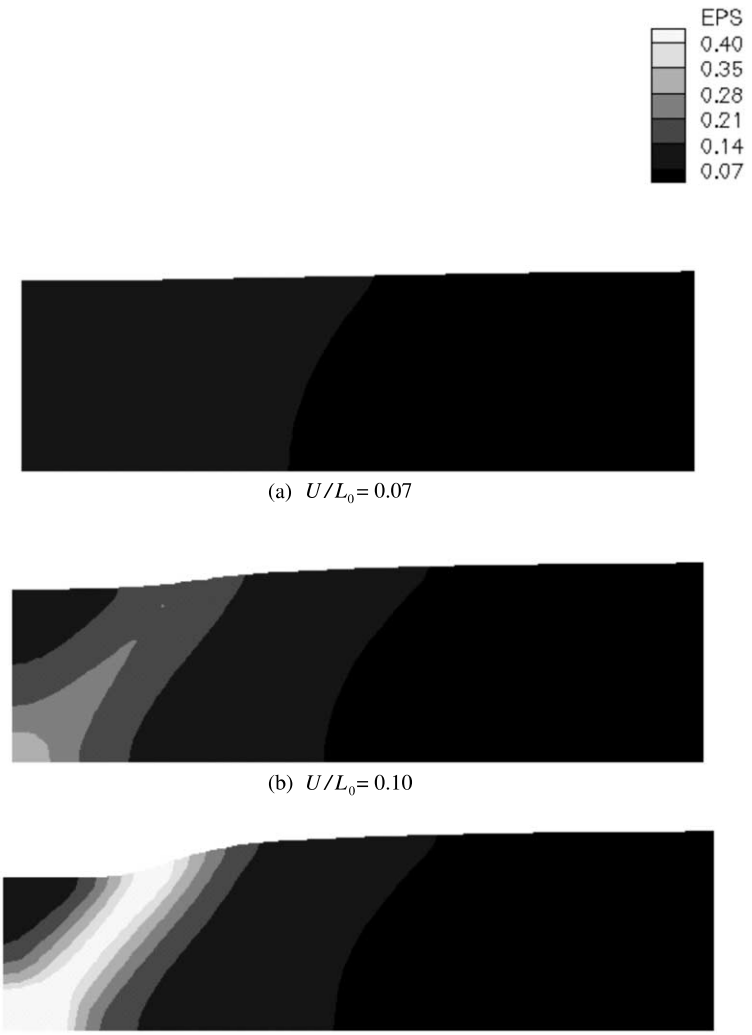

(a) $U/L_0 = 0.07$

(b) $U/L_0 = 0.10$

(c) $U/L_0 = 0.13$

Fig. 6. True strain at various elongation levels.

predicted with element aspect ratios 0.5 and 1.0 are very similar. However, even though the simulations with an element aspect ratio of 2.0 employed more elements than the simulation with an element ratio of 1.0, the shear band predicted with an element aspect ratio of 1.0 is significantly sharper and narrower than the shear band obtained with an element aspect ratio of 2.0. This difference can be explained by the nature of the meshes used in this paper. As described in Section 3.1, our FE meshes are composed of crossed triangles that can resolve narrow shear bands in four directions. If the mesh is not oriented so that one of these directions coincides with the critical orientation for shear bands, then localization can significantly be delayed or entirely suppressed (Tvergaard et al., 1981).

Based on the above observations, it was decided that the relatively fine mesh (16×16 elements in the necking area) with an element aspect ratio of 1 (Fig. 1) would be sufficiently accurate to capture the key features of localized deformation. Thus, this mesh will be used in the simulations discussed henceforth.

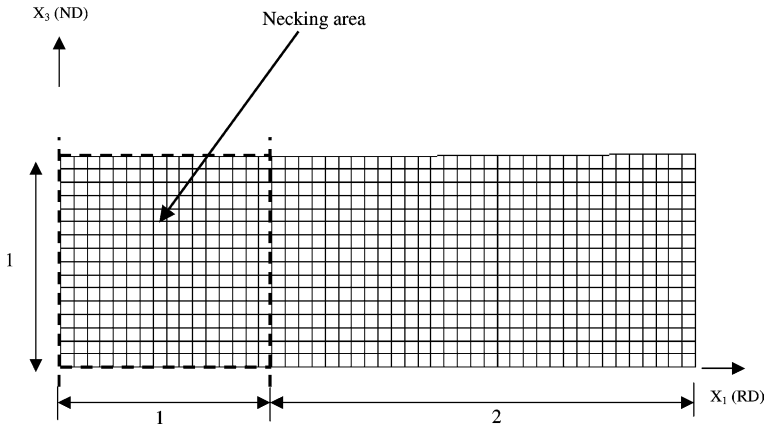

Fig. 7. The necking area considered in mesh sensitivity analyses.

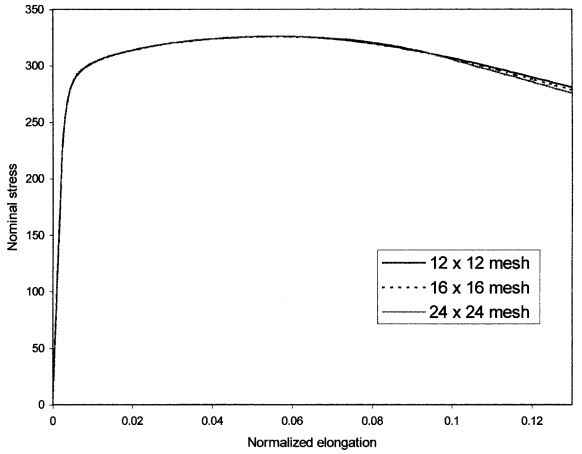

Fig. 8. Nominal stress–normalized elongation curves for three different meshes (at the necking area) with constant element aspect ratio.

4.3. The effect of texture evolution

To investigate the effect of texture evolution on the localization modes, the simulation described above was performed once more, but with texture evolution excluded from the polycrystal model. To prevent texture evolution, the stretching and rotation of the lattice vectors $(\boldsymbol{s}_{(\alpha)}, \boldsymbol{m}_{(\alpha)})$ as described by Eq. (5) were excluded in the numerical analysis. From now on, the model including texture evolution will be referred to as "ITE", while that excluding texture evolution will be referred to as "ETE". Fig. 12 shows that the normalized nominal stress–elongation curves for the two models begin to differ after the maximum normalized nominal stress is attained. In the ITE model, the nominal stress drops faster compared to the ETE model.

The importance of including texture evolution can be seen by comparing Fig. 5c to the deformed mesh of Fig. 13, which results from the ETE simulation at $U/L_0 = 0.13$. As discussed earlier, shear bands are fully developed at this stage of the simulation with the ITE model. However, there are no shear bands formed in

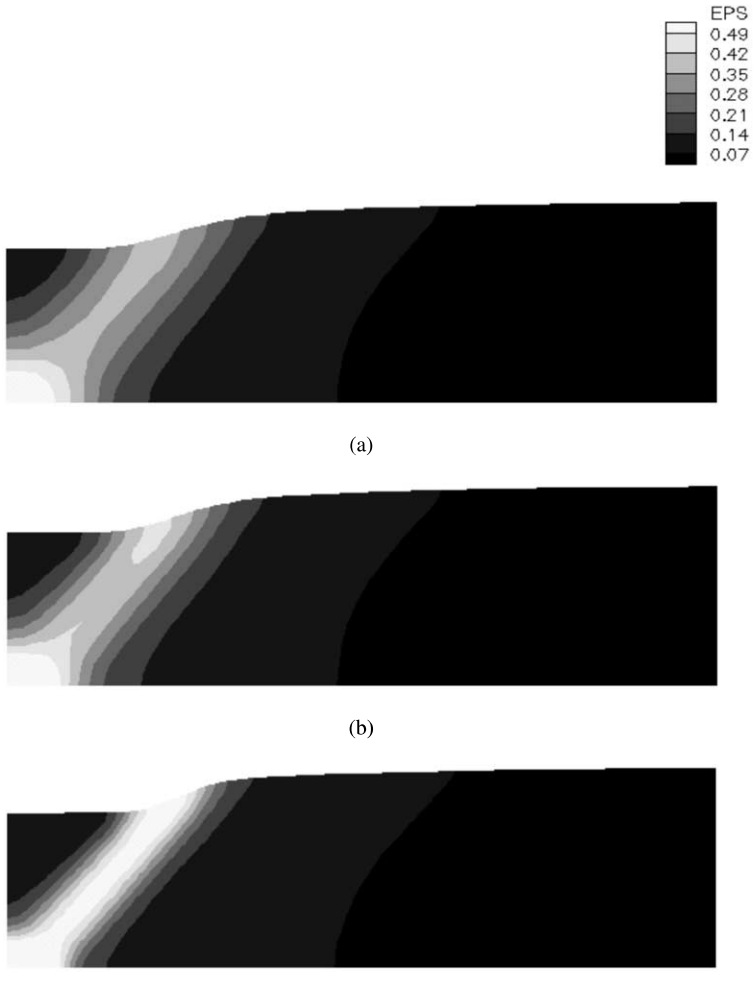

Fig. 9. Contours of true strain (in loading direction) with (a) 12×12 elements, (b) 16×16 elements and (c) 24×24 elements at $U/L_0 = 0.13$.

the ETE model although the initiation of necking is visible. With further loading, strain localizes progressively in the neck area without any formation of shear bands.

Pierce et al. (1982) have shown that, for single crystals, necking causes nonuniform lattice rotations and ''geometrical softening'' that lead to localized shearing. In their work, they have defined ''geometrical softening'' as the increase in the resolved shear stress on the slip system responsible for the concentrated straining. We shall adopt this terminology. As the ETE model does not include texture evolution, necking cannot cause lattice rotations that produce ''geometrical softening''. As a result, although a neck is formed, it cannot act as a triggering mechanism for shear localization in the form of a band.

A comparison between the texture evolutions at the centre of the specimen and at the end of the specimen (away from the neck) is shown in Fig. 14 where the pole figures related to the rolling (x_1) and transverse (x_2) directions are given. Fig. 14a and b correspond to Fig. 6a ($U/L_0 = 0.07$), where initial textures have evolved to a slightly different distribution. However, Fig. 14c and d (corresponding to Fig. 6c;

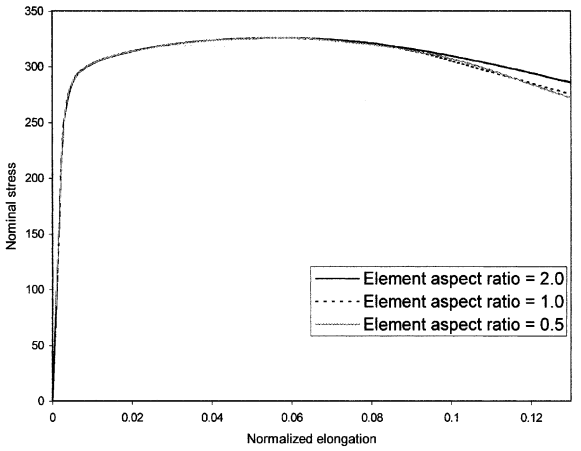

Fig. 10. Nominal stress–normalized elongation curves for three different meshes (at the necking area) with element aspect ratios of 0.5, 1.0 and 2.0.

where $U/L_0 = 0.13$) show that, in the shear band the texture has become much sharper than the texture at the end of the specimen. Texture evolutions for two different elements in the shear band (Fig. 5c) are compared in Fig. 15a and b, which present pole figures related to the rolling (x_1) and normal (x_3) directions for the elements 1 and 2 identified in Fig. 6c, respectively, when $U/L_0 = 0.13$. The differences between these two textures suggest that the deformation modes are different at the selected two elements. Element 1 is undergoing tensile stretching while element 2 is undergoing both shearing and tensile stretching.

4.4. The effect of slip rate sensitivity m

The effect of slip rate sensitivity m on the constitutive response has been investigated by comparing simulations with $m = 0.002$, 0.01 and 0.02 respectively. Fig. 16 compares the normalized nominal stress–elongation curves for these simulations. It can be seen that the normalized nominal stress response increases with increasing m value. It is also noteworthy to mention that, for increasing m, the nominal stress falls much slower from its maximum.

Fig. 17 presents the deformed meshes for the simulation where the rate sensitivity m was taken as 0.02. The normalized extension in Fig. 17a is $U/L_0 = 0.11$ and the deformation pattern is quite uniform. Evidence of the initiation of necking can be seen in Fig. 17b where $U/L_0 = 0.16$ and in Fig. 17c where $U/L_0 = 0.23$, the neck is clearly visible. Note that shear bands were fully developed at $U/L_0 = 0.13$ (Fig. 5c) where the strain-rate sensitivity m was taken as 0.002.

Our results show that when the rate sensitivity was increased, not only does the ductility of the metal increases, but when the rate sensitivity becomes sufficiently high enough (e.g. $m > 0.01$), the localization mode changes from shear bands to necking. This change in the mode of localization was an expected result considering the results of Section 4.3 where the importance of texture evolution on the development of shear bands was clearly demonstrated. Previous studies (Canova et al., 1988) have shown that the rate of texture evolution in tension is decreased by the increase in the slip rate sensitivity. Harren et al. (1989b) have shown for simple shear that, when strain-rate sensitivity m was high enough (0.5 for their material), there was almost no tendency for textures to form. This can be explained by the near vanishing of the plastic spin $\boldsymbol{W}^{\mathrm{p}}$ defined in the second part of Eq. (4) with increasing m. In our simulations, the evolution of texture does not vanish completely when m is taken as 0.02, but the "geometric softening" produced by this texture evolution is not sufficiently high to trigger shear band formation.

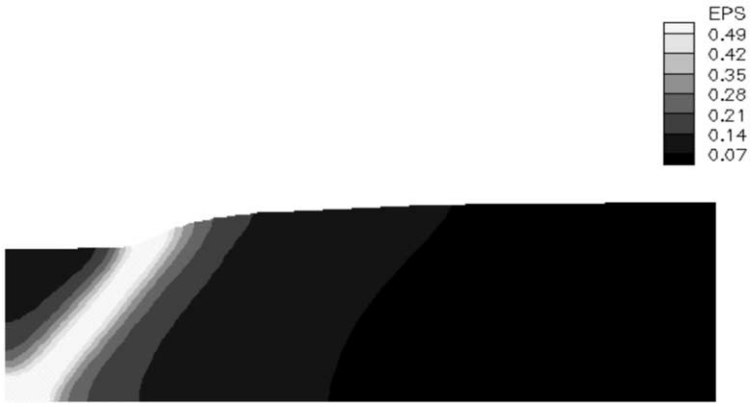

(a) 16 x 32 elements at necking area

(b) 24 x 24 elements at necking area

(c) 32 x 16 elements at necking area

Fig. 11. Contours of true strain (in loading direction) with element aspect ratios of (a) 0.5, (b) 1.0 and (c) 2.0 at $U/L_0 = 0.13$.

The normalized stress σ (σ/σ_{MAX}, where σ refers to the physical component of the true stress in the loading direction calculated at the end section of the specimen, $x_1 = L_0$)–elongation curve is plotted in Fig. 18. It can be seen that σ reaches a maximum around $U/L_0 = 0.09$ (as shown by point B) and then starts to decrease. The normalized elongation ($U/L_0 = 0.058$) where the maximum nominal stress was attained is represented by point A.

The evolution of the neck-section area κ together with the principal logarithmic strain ε (in the rolling direction) at the centre of the specimen is also included in Fig. 18. Our results show that, the attainment of the maximum stress at $U/L_0 = 0.09$ identifies the onset of necking, since $U/L_0 = 0.09$ corresponds to the tapering off of the ε and κ. This conclusion was also reached for different applications of phenomenological plasticity (Tugcu and Neale, 1988; Tugcu, 1991), where their results showed that the attainment of a maximum stress at the end of a round tensile specimen identified the onset of necking.

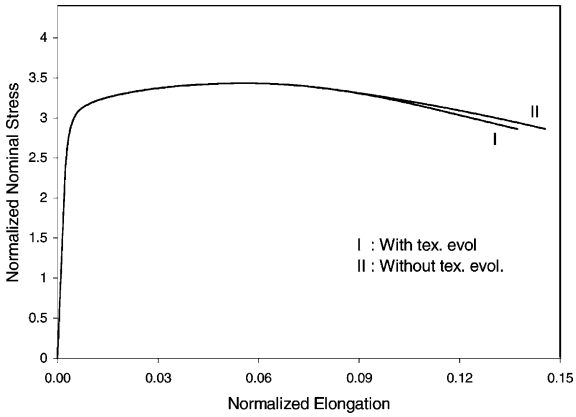

Fig. 12. Comparison between the normalized nominal stress–elongation curves for simulations with and without texture evolution.

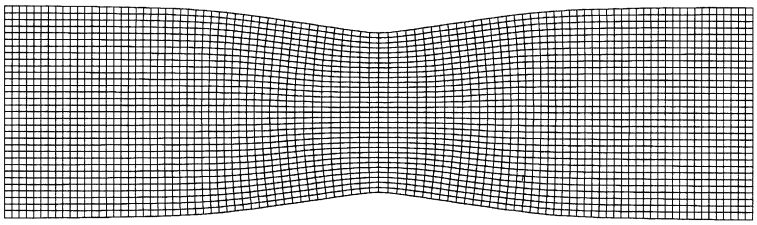

$U/L_0 = 0.13$

Fig. 13. Deformed mesh at $U/L_0 = 0.13$ for the case where texture evolution is excluded.

4.5. The effect of strain hardening

The effect of strain hardening on the formation of shear bands was investigated by comparing the results obtained from simulations with three different values of asymptotic hardening rates; $h_s/\tau_0 = 0$, 0.02 and 0.2. Fig. 19 presents the true stress–true strain curves (for a specimen without imperfection) for these three cases. It can be seen that when $h_s/\tau_0 > 0$ there is strain hardening and when $h_s/\tau_0 = 0$ there is saturation. The normalized nominal stress–elongation curves for these three cases are compared in Fig. 20.

The only difference in the normalized nominal stress–elongation curves for the simulations with $h_s/\tau_0 = 0$ and 0.02 is that the normalized nominal stress drops more rapidly when $h_s/\tau_0 = 0$. Nevertheless, shear bands are still predicted for both cases. However, no shear bands were predicted when the strain hardening rate was taken relatively high ($h_s/\tau_0 = 0.2$) and the specimen deformed with the strain localizing progressively in the neck.

5. Conclusion

A plane-strain crystal plasticity based FE model has been developed to simulate localization modes in polycrystalline solids. The material response of a commercial aluminium alloy (AA3004-H19) was investigated under plane-strain tension.

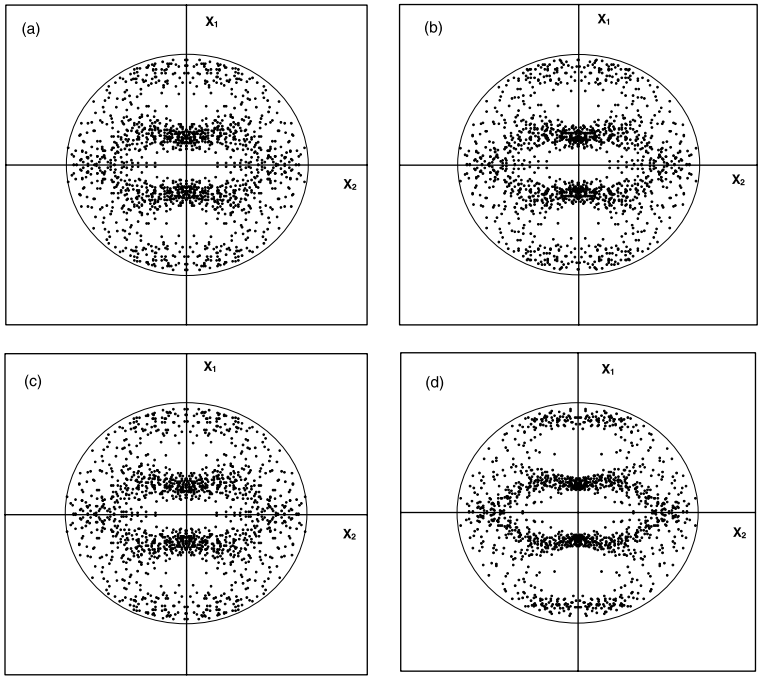

Fig. 14. (a) Texture distribution at the (a, c) end of the specimen, (b, d) centre of the specimen.

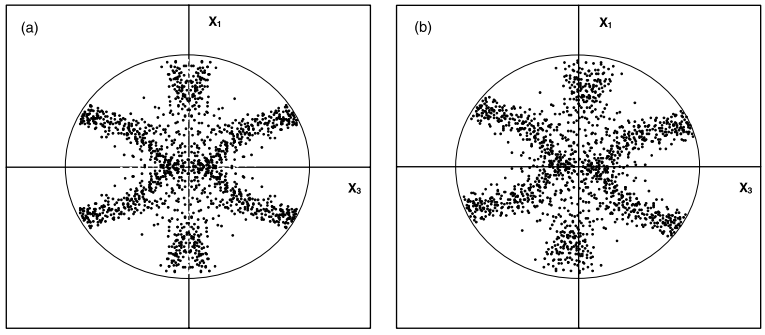

Fig. 15. Texture evolution at element number (a) 1 and (b) 2.

Our simulations showed that localization occurs in two modes. In the first mode, a neck initiates and deformation continues where the strain localizes progressively in this neck. For the rate-dependent analysis considered, the onset of necking is defined by the attainment of the maximum stress at the end section of the specimen, away from the neck. For the limiting case of a rate-independent analysis, this criterion reduces to the attainment of a maximum strain (which is the onset of elastic unloading) since for the rate-independent analysis the attainment of maximum strain will also correspond to the attainment of the maximum stress.

In the second localization mode, necking triggers the formation of shear bands. There are several factors that contribute to the formation and prediction of shear bands such as texture evolution, strain-rate sensitivity and strain hardening.

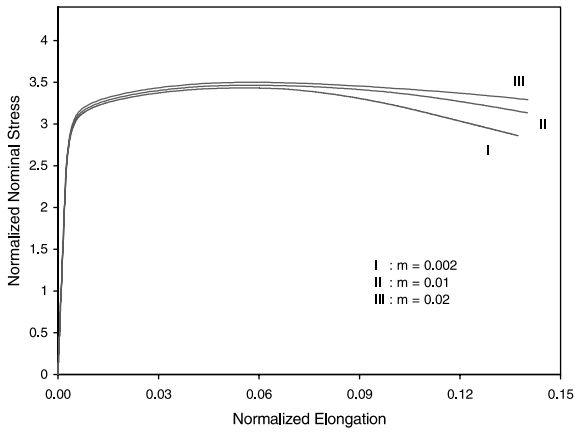

Fig. 16. Normalized nominal stress–elongation curves for various values of the rate sensitivity m.

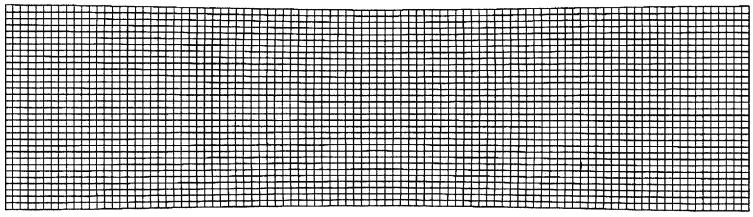

(a) $U/L_0 = 0.11$

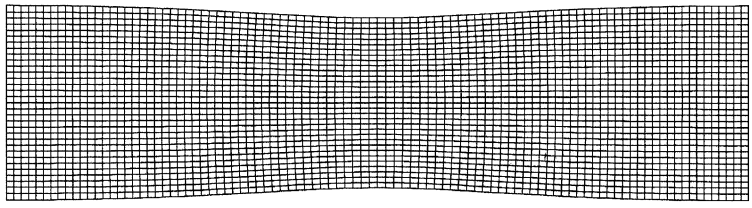

(b) $U/L_0 = 0.16$

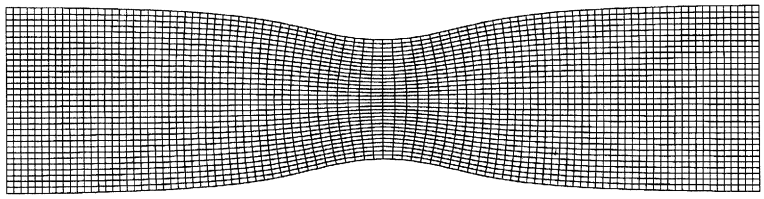

(c) $U/L_0 = 0.23$

Fig. 17. Deformed FE meshes at various elongation levels for the case where $m = 0.02$.

A significant mesh sensitivity effect was not observed on the overall stress response, nor for the initiation and propagation of the localized deformations for those meshes where the element aspect ratios were kept constant. Our results showed that the finer was the mesh, the narrower and sharper became the shear bands. However, the element aspect ratio did affect the prediction of localized deformation; even though the

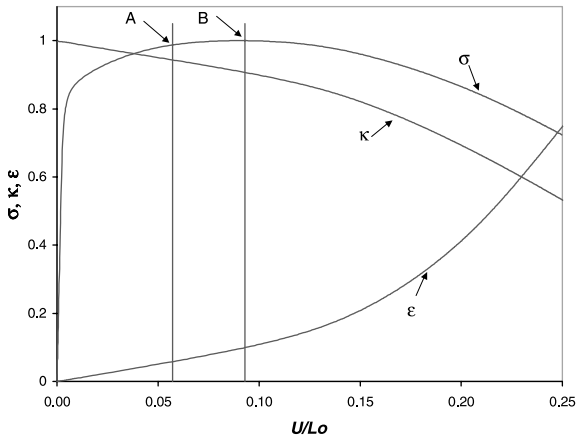

Fig. 18. The evolution of neck section area κ, principal logarithmic strain ε_{11} (at the centre of the specimen) and the true stress σ_{11} (at the end of the specimen).

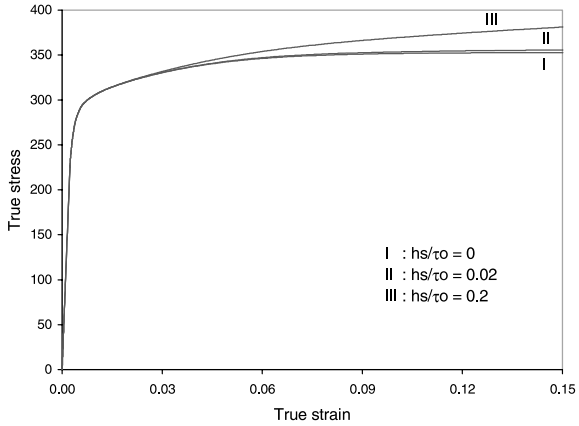

Fig. 19. True stress–strain curves for various asymptotic hardening rates.

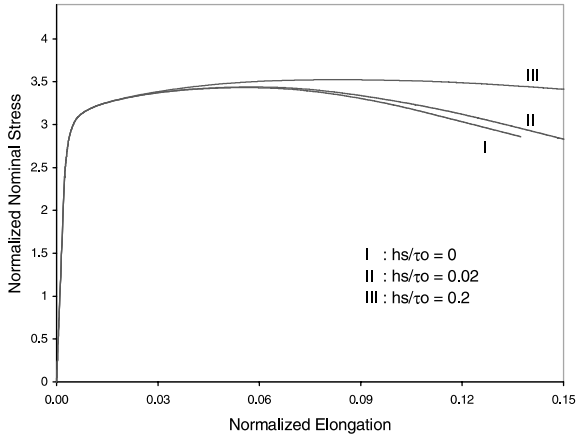

Fig. 20. Normalized nominal stress–elongation curves for various asymptotic hardening rates.

same number of elements was used in both simulations, the shear band predicted with an element aspect ratio of 0.5 was much sharper and narrower than the shear band predicted with an element aspect ratio of 2.0.

Texture evolution was shown to have a very important role in the prediction of shear bands. If texture evolution is not included in the analysis, the "geometric softening" effect that leads to localized shearing does not occur. As a result, shear band formation is precluded from the localization mode. Our simulations have shown that shear bands were formed around an engineering strain of 10%. Although strong textures are not expected to occur at 10% of strain, the evolution of texture at this strain level is still critical in the prediction of shear bands. This effect of texture evolution also explains the inability of phenomenological plasticity models with a smooth yield surface to predict shear bands at realistic strain levels (Tvergaard et al., 1981).

It is well known that increasing the rate sensitivity increases the ductility as it will delay the formation of nonuniform localization modes such as shear bands or necking. Furthermore, our simulations have shown that, when the rate sensitivity was increased to certain values (corresponding to a decrease in the rate of texture evolution), shear band formation was not only delayed, but it was completely precluded from the localization mode since the resulting "geometric softening" was not strong enough to form shear bands.

Strain hardening is another important factor in the formation of shear bands. Our results have shown that strain softening behaviour is not necessarily required to observe shear bands or other localized modes of deformation. However, the rate of strain hardening plays a key role in the determination of the localization mode. When a relatively high rate of strain hardening was considered, shear band formation was completely precluded from the localization mode.

Acknowledgements

This work was supported by the Natural Sciences and Engineering Research Council of Canada (NSERC) and a grant from Alcan International Limited. The authors also gratefully acknowledge the Canadian Foundation for Innovation who funded the acquisition of the IBM SP3 supercomputer, and the Réseau québécois de calcul de haute performance (RQCHP) for their technical support.

References

Asaro, R.J., Needleman, A., 1985. Texture development and strain hardening in rate dependent polycrystals. Acta Metallurgica 33, 923–953.

Beaudoin, A.J., Mathur, K.K., Dawson, P.R., Johnson, G.C., 1993. Three-dimensional deformation process simulation with explicit use of polycrystal plasticity models. International Journal of Plasticity 9, 833–860.

Canova, G.R., Fressengeas, C., Molinari, A., Kocks, U.F., 1988. Effects of rate sensitivity on slip system activity and lattice rotation. Acta Metallurgica 36, 1961–1970.

Chang, Y.W., Asaro, R.J., 1981. An experimental study of shear localization in aluminum–copper single crystals. Acta Metallurgica 29, 241–254.

Harren, S.V., Asaro, R.J., 1989a. Nonuniform deformations in polycrystals and aspects of the validity of the Taylor Model. Journal of the Mechanics and Physics of Solids 37, 191–232.

Harren, S.V., Dève, H.E., Asaro, R.J., 1988. Shear band formation in plane strain compression. Acta Metallurgica 9, 2435–2480.

Harren, S.V., Lowe, T.C., Asaro, R.J., Needleman, A., 1989b. Analysis of large-strain shear in rate-dependent face-centred cubic polycrystals: correlation of micro- and macromechanics. Philosophical Transactions of the Royal Society of London A 328, 443–500.

Hutchinson, J.W., Neale, K.W., 1977. Influence of strain-rate sensitivity on necking under uniaxial tension. Acta Metallurgica 25, 839–846.

Hutchinson, J.W., Neale, K.W., 1978a. Sheet necking. II. Time-independent behaviour. In: Koistinen, D.P., Wang, N.M. (Eds.), Mechanics of Sheet Metal Forming. Plenum Press, New York, pp. 127–153.

Hutchinson, J.W., Neale, K.W., 1978b. Sheet necking. III. Strain-rate effects. In: Koistinen, D.P., Wang, N.M. (Eds.), Mechanics of Sheet Metal Forming. Plenum Press, New York, pp. 269–285.

Inal, K., Wu, P.D., Neale, K.W., 2000a. Simulation of earing in textured aluminum sheets. International Journal of Plasticity 16, 635–648.

Inal, K., Wu, P.D., Neale, K.W., MacEwen, S.R., 2000b. Numerical simulation of large deformation polycrystalline plasticity. In: Martin, P., MacEwen, S.R., Verreman, Y., Liu, W., Goldak, J. (Eds.), Mathematical Modelling in Metal Processing and Manufacturing—COM2000. Ottawa.

Kalidindi, S.R., Anand, L., 1994. Macroscopic shape change and evolution of crystallographic texture in pre-textured fcc metals. Journal of the Mechanics and Physics of Solids 42, 459–490.

Kalidindi, S.R., Bronkhorst, C.A., Anand, L., 1991. On the accuracy of the Taylor Assumption in polycrystalline plasticity. In: Boehler, J.P., Khan, A.S. (Eds.), Anisotropy and Localization of Plastic Deformation, Proceedings of Plasticity '91: The Third International Symposium on Plasticity and its Current Applications. Elsevier, London, pp. 139–142.

Needleman, A., 1988. Material rate dependence and mesh sensitivity in localization problems. Computer Methods in Applied Mechanics and Engineering 67, 69–85.

Needleman, A., Tvergaard, V., 1984. Finite element analysis of localization in plasticity. In: Oden, J.T., Carey, G.F. (Eds.), Finite Elements—Special Problems in Solid Mechanics. Prentice Hall, Englewood Cliffs, pp. 94–157.

Peirce, D., Asaro, R.J., Needleman, A., 1982. An analysis of nonuniform and localized deformation in ductile single crystals. Acta Metallurgica 30, 1087–1119.

Peirce, D., Asaro, R.J., Needleman, A., 1983. Material rate dependence and localized deformation in crystalline solids. Acta Metallurgica 31, 1951–1976.

Sorensen, N.J., Andersen, B.S., 1995. A parallel finite element method for the analysis of crystalline solids. DCAMM Report, The Technical University of Denmark.

Tugcu, P., 1991. Tensile instability in a round bar including the effect of material strain-rate sensitivity. Computer Methods in Applied Mechanics and Engineering 93, 335–351.

Tugcu, P., Neale, K.W., 1988. Analysis of neck propagation in polymeric fibres including the effects of viscoplasticity. Journal of Engineering Materials and Technology ASME 110, 395–400.

Tvergaard, V., Needleman, A., Lo, K.K., 1981. Flow localization in the plane strain tensile test. Journal of the Mechanics and Physics of Solids 29, 115–142.

Van der Giessen, E., Neale, K.W., 1993. Analysis of the inverse swift effect using a rate-sensitive polycrystal model. Computer Methods in Applied Mechanics and Engineering 103, 291–313.

Wu, P.D., Neale, K.W., Van der Giessen, E., 1996a. Simulation of the behaviour of FCC polycrystals during reversed torsion. International Journal of Plasticity 12, 1199–1219.

Wu, P.D., Van der Giessen, E., 1996b. Computational aspects of localized deformations in amorphous glassy polymers. European Journal of Mechanics A/Solids 15, 799–823.

Wu, P.D., Neale, K.W., Van der Giessen, E. 1997. On crystal plasticity FLD analysis. Proceedings of the Royal Society of London 453, 1831–1848.

Zhu, Z.G., Batra, R.C., 1993. Analysis of dynamic shear bands in an FCC single crystal. International Journal of Plasticity 9, 653–696.

Zikry, M.A., Nemat-Nasser, S., 1990. High strain-rate localization and failure of crystalline materials. Mechanics of Materials 10, 215–237.